

**Thermo-osmotic Ionogel enabled High-efficiency Harvesting
of Low-grade Heat**

Journal:	<i>Journal of Materials Chemistry A</i>
Manuscript ID	TA-ART-03-2021-001836.R1
Article Type:	Paper
Date Submitted by the Author:	03-Jun-2021
Complete List of Authors:	Li, Wei; Texas A&M University College Station, Materials Science Liu, Yuchen; Texas A&M University College Station, Materials Science Zhang, Zimeng; Texas A&M University College Station, Materials Science Liu, Ruochen; Texas A&M University College Station, Materials Science Qiu, Jenny; Texas Tech University, Wang, Shiren; Texas A&M University College Station, Materials Science

Thermo-osmotic Ionogel enabled High-efficiency Harvesting of Low-grade Heat

Wei Li,^a Yuchen Liu,^a Zimeng Zhang,^a Ruochen Liu,^b Jingjing Qiu,^c Shiren Wang^{*a,b}

^aDepartment of Industrial and Systems Engineering, Texas A&M University, College Station, TX 77843, United States.

^bDepartment of Materials Science and Engineering, Texas A&M University, College Station, TX 77843, United States.

^cDepartment of Mechanical Engineering, Texas Tech University, Lubbock, TX 79409, United States.

*Correspondence to: s.wang@tamu.edu

Abstract

Low efficiency in recovering low-grade heat remains unresolved despite decades' attempts. In this research, we designed and fabricated a novel thermo-osmotic ionogel (TOI) composite to recover low-grade heat to generate electric power through thermo-induced ion gradient and selective ion diffusion. The TOI composite was assembled with crystalline ionogel (polymer-confined $\text{LiNO}_3 \cdot 3\text{H}_2\text{O}$) film, ion selective membrane, and hydrogel film. With a 90 °C heat supply, the single TOI composite produced a high open-circuit voltage of 0.52 V, a differential thermal voltage of ~26 mV/K, a peak power density of 0.4 W/m², and a ground-breaking peak energy conversion efficiency of 11.17%. Eight pieces of such TOI composite were connected in series, demonstrating an open-circuit voltage of 3.25 volts. Such a TOI system was also demonstrated to harvest body temperature for powering a LED, opening numerous opportunities in powering wearable devices.

Introduction

A huge amount of low-grade heat (below 100 °C) is widely available from natural resources or industries¹⁻³. Natural low-grade heat like solar spectrum and geothermal activity exceeds the annual global energy consumption⁴⁻⁷. In global industrial production, 72% of the primary energy consumption is wasted as low-grade heat^{1,8}. Numerous efforts for harvesting such low-grade heat have been made in the past decades, but the recovery efficiency is still very low, and thus their power generation potential remains unexplored⁹. For example, current thermoelectrics (TEs) showed <4.1% recovering efficiency due to material constraints¹⁰⁻¹². Pyroelectric energy conversion showed <3.8% recovering efficiency, in which producing temperature oscillations is extremely challenging^{13,14}. Liquid thermo-electrochemical systems^{8,15-19} also showed a recovery efficiency <5.7% for such low-grade heat^{3,5}, where inefficient thermo-driven ion diffusion is the main limitation.

Our theoretical calculations, as shown in Fig. 1a, indicate osmotic potential driven-ion diffusion is >100 times more efficient than thermo-driven ion diffusion (supplementary text 1)^{20,21}. Actually, the efficiency of direct converting osmotic potential into electric energy²²⁻²⁴ was reported as high as 44.2%²⁵⁻²⁸, around 10-fold higher than the aforementioned thermo-electric energy conversion efficiencies. Therefore, integrating heat recovery into ion gradient-based power generation is likely to be more efficient than direct low-grade heat recovery. However, how to effectively integrate thermal energy with ion gradient generation is a big challenge. Waste heat has been used to vaporize saline water based on membrane distillation to create a salinity gradient for power generation²⁹⁻³². Due to extremely low efficiency in the thermo-vapor conversions, the overall heat recovery efficiency was <1.5%. Low-grade heat has also been used to tune the salt solubility for the generation of saline gradient and thereby the generation of electric power, but the overall efficiency was <2%^{18,33-35}. Efficient conversion of low-grade heat into ion gradient is vital to efficiently harvest low-grade heat.

In this research, we present an innovative thermo-osmotic ionogel (TOI) approach to efficiently harvest low-grade heat for power generation (as illustrated in Fig. 1b and fig. S1). Waste heat drives the

phase transition of flexible ionic crystal to produce ion gradient, subsequent selective ion diffusion/separation, and thus electricity. As a result, we demonstrated a ground-breaking peak efficiency of 11.17% in converting low-grade heat to electric energy. Specifically, the TOI composite consists of a thin layer of ionogel made from polyacrylamide (PAM) and crystalline lithium nitrate trihydrate (LNT, $\text{LiNO}_3 \cdot 3\text{H}_2\text{O}$), a cation selective membrane, and a hydrogel film with 0.1M LiNO_3 . $\text{LiNO}_3 \cdot 3\text{H}_2\text{O}$ was employed as the ionic crystalline salt due to its low melting temperature and high ionic conductivity³⁶. The heat is firstly absorbed to melt crystalline $\text{LiNO}_3 \cdot 3\text{H}_2\text{O}$, resulting in free Li^+ and NO_3^- ions (figs. S2, S3a, and S3B) and thereby creating a high ion gradient between the ionogel and hydrogel. With the aid of cation exchange membrane (CEM) and hydrophilic polymer chains in ionogel, the thermally induced ion gradient drives the cations to diffuse selectively from the high-salinity ionogel (HSI) to the low-salinity hydrogel (LSH), resulting in the separated anions in the ionogel and separated cations in the hydrogel. When two symmetrical electrodes (such as platinum (Pt) and carbon fiber cloth (CFC)) are attached, cations accumulate at the cold-side hydrogel-electrode interface while anions gather at the hot-side ionogel-electrode boundary, leading to a significant electrochemical potential between the two electrodes (fig. S3c). When an external electrical load is connected to the capacitive electrodes, an electric current could be generated, converting the electrochemical potential to electric energy (fig. S3d). The ionogel could recrystallize as long as its temperature drops below the recrystallization temperature of $\text{LiNO}_3 \cdot 3\text{H}_2\text{O}$, causing a much lower Li^+ concentration in the ionogel than in the hydrogel. The resultant reverse ion gradient could cause Li^+ to move back to the ionogel layer from the hydrogel layer, resulting in the reformation of crystalline $\text{LiNO}_3 \cdot 3\text{H}_2\text{O}$ (figs. S3e and S3f). Consequently, the TOI composite recovers to its original state (fig. S3a).

Fig. 1. Concept and working principle of the TOI approach. (a) Comparison of ion flow rate driven by ion gradient (Δc) and temperature gradient (ΔT). The results are calculated based on the Soret coefficient, where Δc is produced between $\text{LiNO}_3 \cdot 3\text{H}_2\text{O}$ (18.4 mol/kg) and 0.1 M LiNO_3 solution. x represents the thickness of the separation membrane. J_C and J_T are the ion flow rate driven by Δc and ΔT , respectively. (b) Illustration of a proposed TOI composite, which converts low-grade heat into Δc by melting the crystalline salt hydrate, and then generates electric energy through ion diffusion and selective permeation.

Experimental

Materials

Reagents for the ionogel and hydrogel synthesis, including lithium nitrate (LiNO_3), acrylamide (AM), N, N'-methylene-bisacrylamide (MBA), Ammonium persulfate (APS) and N, N, N', N'-Tetramethylethylenediamine (TEMED), were purchased from Sigma-Aldrich Co., Ltd. The cation exchange membrane (CEM, Fumapem F-930) and carbon fiber cloth were purchased from Fuel Cell Store Company. CEM is a long side-chain perfluorinated sulfonic acid (LSC-PFSA) with low resistance and high cation selectivity. CEM was activated by soaking in a 5 wt% H_2SO_4 solution at 95 °C for at least 24h and then soaked in DI water until pH=7. All conventional chemicals were of analytical grade and employed without further purification.

Methods

Ionogel and hydrogel synthesis. The ionogel was prepared via the solution-cast method³⁷. First, lithium nitrate solution with certain molarity (18.4 mol/kg for high-salinity $\text{LiNO}_3 \cdot 3\text{H}_2\text{O}$ ionogel, 0.1 mol/kg for low-salinity hydrogel) was prepared by mixing anhydrous lithium nitrate with stoichiometric amounts of deionized water and heated to 50 °C to create homogenous liquid. Then, the gel agents including monomer AM (5, 10, or 20 wt% of salt solution) and cross-linker MBA (0.02 molar ratio of AM) were added to the

salt solution and treated with ultrasonication until became completely homogeneous. Afterward, the polymerization initiator APS (0.01 molar ratio of AM) and catalyst TEMED (0.01 molar ratio of AM) were added into the mixture under thoroughly stirring to get a homogeneous solution. Finally, the mixture was poured into a silicone mold and kept at 60 °C for complete polymerization to obtain quasi-solid ionogels or hydrogels.

Thermal characterization. The thermal properties of the ionogels were investigated by DSC (Q20, TA Instrument), with a test temperature range from -50 to 95 °C. We tested 5 cyclic melting-recrystallization phase transitions of the ionogel to explore the reversibility of the ionogel. The melting point, specific heat, and enthalpy of melting can be extracted from the recorded heat flux, time, and temperature relationships. Specifically, the enthalpy is proportional to the area under the heat flux curve. The thermal conductivity of the ionogel and hydrogel was measured using a laser flash apparatus (LFA 457, NETZSCH). The detailed information can be found in fig. S12. The thermal conductivity κ is then calculated by $\kappa = \alpha \rho C_p$, in which κ is the thermal diffusivity, ρ is the density and C_p is the heat capacity.

Ionic conductivity measurement. Electrochemical impedance spectroscopy measurements (EIS) were carried out to determine the ionic conductivity of the ionogels. The ionogel samples were sandwiched between two square platinum (Pt) electrodes with a size of 14*14 mm. In order to test the ionic conductivity of the sample at different temperatures, we attached a polyimide heating film to the bottom surface of the sample as a heat source. A T-type thermocouple (TC-200) was employed to monitor the temperature of the center of the sample. With an excitation voltage of 5 mV, the electrochemical workstation (CHI 660D, CH Instruments) was used to measure the impedance of ionogel in the frequency range of 1 Hz to 1 MHz³⁸. Software EisAnalyser (EIS Spectrum Analyser) was used to fit the impedance data with Randles equivalent circuit (fig. S7a), which is composed of an electrolyte resistance (R_e) in series with the parallel combination of a constant phase element (CPE) and a charge transfer resistance (R_{ct})³⁸.

The effective ionic conductivity σ_e was calculated using $\sigma_e = \frac{\Delta x}{R_e A}$, where A is the cross-sectional area of the sample, Δx is the distance between the electrodes. In the fitting model, R_e is the real impedance at the frequency where the dielectric loss tangent ($\tan \psi = \frac{\epsilon''}{\epsilon'}$) reaches its maximum value, corresponding with the minimum value of Z'' in the Nyquist diagram ($-Z''$ vs Z')³⁹. A similar method was used to measure the ionic conductivity of LiNO₃ solutions, in which the solutions and electrodes were sealed in a cuboid container. As for the ionogel, R_e is the Z' of the Nyquist diagram at around 100k HZ. Thus, the real-time ionic conductivity of crystalline LiNO₃-3H₂O ionogel during the melting process (Fig. 3c) was measured by recording the real-time Z' with an alternating frequency of 100k HZ.

Mechanical test. Tensile and compression tests were performed at room temperature with a universal tensile machine (Instron model 3345). During the test, the LiNO₃-3H₂O in the ionogel remained in a molten state. Dogbone samples of ionogels and hydrogels for tensile testing were cast with a modified dimension of the ASME VSM-5 standard model. The cross-section area of the dogbone samples was measured by caliper before testing, and sandpaper was used to prevent slippage during the measurement. The tensile testing speed was set to 5 mm/min. The cuboid sample with a height of 9 mm, a length of 14 mm, and a width of 14 mm was used for compression testing at a speed of 3 mm/min.

Electric power generation characterization of the TOI cell. A typical TOI cell was assembled by layering low-salinity hydrogel (LSH), CEM, and crystalline high-salinity ionogel (HSI) layer in an insulated mold (Figs.

S2 and S3). Two symmetric electrodes such as Pt were connected to LSH and HSI. Temperature-adjustable polyimide heater film was employed as the heat source on one side. The other side was passively cooled down in the air. Two T-type thermocouples were employed to monitor the temperature of hot-side HSI and cold-side LSH. Once heating, the crystalline $\text{LiNO}_3 \cdot 3\text{H}_2\text{O}$ in ionogel would melt and generate an ion gradient with the neighboring hydrogel. The electrical voltage between electrodes was real-time recorded by a Keithley 2182A Nanovoltmeter or a Fluke 117 Multimeter (Fig. S3). The current was recorded using a CHI 660D workstation or a Keithley 2400. A Decade resistance box was connected to the circuit to test the electric power generation of the TOI approach under various external loads. The differential thermal voltage of the TOI cell was calculated by $\frac{V_{oc}}{\Delta T}$, where V_{oc} is the measured open-circuit voltage between the two electrodes, and ΔT is the measured temperature difference between the electrodes².

Energy conversion efficiency calculation of the TOI cell. The calculation methods for heat-to-electric energy conversion efficiency (η_E) of the TOI composite were described in Supplementary Text 1 to 3. For better comparison with the reported literature, Carnot-relative efficiency was provided as the ratio of η_E to η_{Carnot} . Specifically, the Carnot efficiency of the TOI was calculated by $\eta_{Carnot} = \frac{\Delta T}{T_H + 273.15} = \frac{T_H - T_M}{T_H + 273.15}$, where T_H is the temperature of the ionogel-end of TOI, T_M is the melting point of the ionogel. The heat input of the TOI consisted of the heat absorbed in the ion generation stage and the diffusion heat in the power generation, and the TOI kept at the melting point to generate an ion gradient before starting to generate power. The power generation was also a synergistic effect of ΔT and Δc . Thus, the melting point ($T_M=28^\circ\text{C}$) was taken as the T_L to calculate the Carnot efficiency. A heat source above the melting point can activate the TOI to generate power.

Results and discussion

Thermally-induced ion gradient

We firstly examined the polymer confinement effect on the enthalpy of ionic crystal transition. The inclusion of polymer chains can disrupt the crystal structure of the crystalline salt hydrate and form intermolecular bonds with free ions^{40, 41}, so it is likely to help reduce the enthalpy of melting (ΔH) for high heat-ion gradient conversion efficiency. $\text{LiNO}_3 \cdot 3\text{H}_2\text{O}$ was dissolved into acrylamide monomer solution, and in-situ polymerization led to polymer chains confined ionic crystals, namely the ionogel. As shown in the differential scanning calorimetry (DSC) results (Fig. 2a), when the PAM inclusion was less than 10 wt%, the normalized melting enthalpy of $\text{LiNO}_3 \cdot 3\text{H}_2\text{O}$ was decreased with the increase of PAM concentration. The enthalpy was then increased a little bit at 20 wt% PAM, which may be caused by more sensible heat absorption during the melting process.

Fig. 2. Characterization of ionogels and heat-induced ion gradient generation. (a) DSC curve and normalized melting enthalpy of $\text{LiNO}_3 \cdot 3\text{H}_2\text{O}$ in ionogels with various PAM concentrations. (b) Ionic conductivity and tensile strength of $\text{LiNO}_3 \cdot 3\text{H}_2\text{O}$ ionogel as a function of PAM concentrations. (c) The real-time phase transition and ion generation of crystalline $\text{LiNO}_3 \cdot 3\text{H}_2\text{O}$ ionogel as a function of heating time and temperature (Left insert: unheated crystalline ionogel, Right inset: heated molten ionogel). (d) Measured and fitted impedance spectra of the 0.1M LiNO_3 hydrogel, $\text{LiNO}_3 \cdot 3\text{H}_2\text{O}$ ionogel, and ionogel/CEM/hydrogel composite at 45°C . The inset shows the zoomed view in the high-frequency region.

Furthermore, the ion gradient was determined by the ratio of effective ion concentration (γC , where γ is the ionic activity coefficient and C is the salt concentration) between the ionogel and hydrogel. γ decreases with an increasing C since the mobility of cation and anion is restricted due to the increasing ion pairs formation⁴². The ionic conductivity ($\sigma = \frac{F^2}{RT} \sum z_i^2 \gamma_{ci} C_i D_i$, where D_i and z_i represent the diffusion coefficient and the charge of carriers of the i specie, respectively) showed a positive linear relationship with γC , and thus it was taken as an indicator of γC in this study.

The ionic conductivity of salt hydrate and ionogels was investigated via alternating current impedance spectroscopy measurements. As the temperature was increased from 20 °C to 45 °C, the pure $\text{LiNO}_3 \cdot 3\text{H}_2\text{O}$ transitioned from crystalline solid to liquid, resulting in ionic conductivity of 8 S/m. This result is well consistent with the reported value³⁶. The introduction of porous PAM networks into the $\text{LiNO}_3 \cdot 3\text{H}_2\text{O}$ can dissociate $\text{Li}^+ \cdot \text{NO}_3^-$ ion pairs by forming hydrogen bonding with NO_3^- , and thereby improving the ionic conductivity and effective ion concentration in the ionogel⁴³. At 5 wt% of the PAM polymer addition, the ionic conductivity of $\text{LiNO}_3 \cdot 3\text{H}_2\text{O}$ ionogel was 17.7 S/m at 45 °C (Fig. 2b), which was almost twice that of the pure $\text{LiNO}_3 \cdot 3\text{H}_2\text{O}$ (fig. S4). The ionic conductivity of ionogels decreased at >5 wt% of PAM fractions due to the increased steric effect of PAM networks, which limited the transport of free ions. On the other hand, the mechanical performance (such as tensile and compression strength) of the ionogel (salt hydrate in molten state) increased with the increasing PAM content (Fig. 2b and fig. S5), which helps to achieve a better ionogel/CEM/hydrogel interface by pressurizing TOI composite. Taking account of the enthalpy of melting, ionic conductivity, and mechanical performance together, a polymer content of 10 wt% was chosen in the following work. To balance between ionic conductivity and the ion gradient, the salt concentration for low-salinity hydrogel was set to 0.1 mol/kg, and the ionic conductivity was 1.1 S/m at 45 °C (fig. S6).

In addition to the polymer chain interactions, an elevated temperature can also help dissociate ion pairs and increase the ion diffusion coefficient²¹, and thus ionic conductivity, and effective ion concentration. When the crystalline $\text{LiNO}_3 \cdot 3\text{H}_2\text{O}$ ionogel (white ionogel, the left inset in Fig. 2c) was heated, free lithium and nitrate ions were generated. Due to the confinement of crosslinked polymer chains, the molten ionogel can maintain the gel-state (translucent ionogel, the right inset in Fig. 2c). Considering that the γC of ionogel is proportional to the ionic conductivity, the phase transition and ion generation process of crystalline ionogel can be qualitatively represented by the ionic conductivity of the ionogel as a function of temperature and time (Fig. 2c). When the $\text{LiNO}_3 \cdot 3\text{H}_2\text{O}$ ionogel was heated from 18 to 40 °C within 1 hour, the ionic conductivity increased almost 10 folds.

The Nyquist plots of the 0.1M LiNO_3 hydrogel, $\text{LiNO}_3 \cdot 3\text{H}_2\text{O}$ ionogel, and ionogel/CEM/hydrogel composite were fitted by the Randle equivalent circuit (Fig. 2d). At a low-frequency region, ionogel/CEM/hydrogel composite shows a smaller finite-length Warburg (fig. S7), indicating a limited diffusion layer and ideal reservoir at the boundary⁴⁴. Obviously, there exists a spontaneous ion diffusion from the ionogel to hydrogel due to the ion gradient.

Electric power generation

Thermally-induced ion gradient and immediately selective ion diffusion led to the accumulation of cation near the cold-side hydrogel, thereby generating an electric field from the cold-end to the hot-end. Hence, the voltage generated by the ion redistribution in the TOI composite can be

measured². The temperature of the hot/cold end of the TOI composite was real-time monitored by thermocouples. With an 88 °C heat source, the TOI composite absorbed heat to melt crystalline LiNO₃·3H₂O ionogel and produced mobile ions in the first 20 minutes, in which the ionogel was maintained at the melting temperature (Fig. 3a). Once the crystalline ionogel melted and generated a high ion gradient with the adjacent hydrogel, the ions would diffuse from ionogel to hydrogel selectively and spontaneously. During this process, the temperature of hot-side ionogel rose to near the source temperature (T_H) and generated a ΔT of around 18 °C with the cold-side. The V_{OC} reached a near saturation value of 0.48 V in about 1 hour, which was much larger than the previously reported voltage achieved by thermally driven liquid thermo-electrochemical systems or TEs^{3, 5, 10}.

Fig. 3. Electrical power generation of TOI composite. (a) Real-time recording of the V_{OC} and hot/cold side temperature of TOI composite as the heat source stayed at 88 °C. (b) Voltage generation mechanism of the TOI approach, osmotic-driven and thermo-driven ion diffusion integrated with selective permeation. The enhanced cation selectivity of the TOI system is ascribed to the intermolecular hydrogen bonding between nitrate anion and densely hydrophilic amide group, along with the thermo-mobility difference of nitrate anion and lithium cation. (c) V_{OC} and differential thermal voltage of TOI composite as a function of the temperature of heat source. (d) Short-circuit current of TOI system as a function of time during discharging. (e) Current of the discharge process at the different external resistors. The inset shows the measurement circuit. (f) Corresponding output voltage and peak power density at the different external resistors.

The open-circuit voltage of TOI composite is contributed by the synergy of osmotic-diffusion (E_{OD}) and thermo-diffusion (E_{TD}) of ions (Fig. 3b). To clarify the role of osmotic-diffusion, we measured the voltage of the liquid TOI system (LiNO₃·3H₂O solution/CEM/0.1M LiNO₃ solution configuration) and TOI composite (gel-state) in an isothermal condition (35 °C, without ΔT). The measured V_{OC} of the liquid TOI system was around 0.1 V, highly consistent with the previously reported value in the osmotic power generation system^{22, 26}. The V_{OC} of the TOI composite was measured to 0.21 V, much higher than 0.1 V of the liquid TOI system (Table S3). The improvement in the osmotic-driven voltage of the gel-state TOI composite is ascribed to the dense hydrophilic amide groups of the PAM polymer in the ionogel, which can form intermolecular hydrogen bonding with the nitrite anions and hinder their diffusion, thereby enhancing the ion selectivity of the TOI composite. When the temperature of the heat source is higher, ΔT is generated, and the voltage is further boosted by the thermo-diffusive thermopower based on the Soret effect. At a ΔT of 15.75 °C, a single LiNO₃·3H₂O ionogel film can generate a voltage of 0.166 V, indicating a thermopower of 10.5 mV/K (Table S3). Similarly, the single hydrogel film containing 0.1M LiNO₃ also contributes a thermopower of 5.5 mV/K due to the selective thermo-diffusion of Li⁺ and H⁺. In the TOI composite, the aforementioned ion separation mechanism synergistically causes a series voltage effect and generates a higher V_{OC} . With the heat source of 47 °C, a ΔT of 10 °C was built within the TOI composite, resulting in a voltage of 0.267 V (Fig. 3c). As the heat source temperature continued to rise, the effective ion concentration in the ionogel increased, leading to a larger ion gradient along with a larger ΔT . When the heat source reached 90 °C, the ΔT was around 20 °C and the measured V_{OC} was 0.524 V. The differential thermal voltage (analogous to thermopower) was derived by dividing the obtained thermally generated V_{OC} by the ΔT across the electrodes². The differential thermal voltage of the TOI composite was 18 mV/K at 40 °C, and increased slightly to 26 mV/K at 90 °C. Compared with other widely reported thermoelectric

ionogels, the differential thermal voltage of TOI composites is comparable to that of ionic liquid ionogels based on the Soret effect (26.1 mV/K)^{45, 46}, but greater than that of redox-active ionogels based on the thermocouple effect (several mV/K)⁴⁷.

Once the Pt electrode was connected by the circuit under a supply heat of 90 °C, the transient short circuit current (I_{SC}) was measured to be 0.09 mA, but it decreased rapidly to 0.023 mA in 15 minutes (Fig. 3d). After that, I_{SC} continued to decrease slowly to 0.002 mA in 60 minutes. The transient current is positively correlated with the temperature of the heat source because a higher heat source temperature leads to faster ion mobility and larger thermo-driven voltage. When the heat source was removed, the current continued to drop, even to a negative value. It was because the molten $\text{LiNO}_3\cdot 3\text{H}_2\text{O}$ in the ionogel would recrystallize and made the concentration of cation in the ionogel lower than that in the hydrogel, which caused back diffusion of cations from hydrogel to ionogel, making it possible to reactivate the TOI composite.

The discharging current of TOI composite is a result of the non-faradaic process caused by the capacitive desorption of ions on ionogel/anode and hydrogel/cathode interface (fig. S9)^{48, 49}, and thus the discharging process will stop as the electrodes are fully polarized. Of course, the electrode with a large specific surface area, such as porous carbon-based materials, can further improve capacitive electron capacity^{50, 51}. For example, the peak I_{SC} density of the TOI system with carbon fiber cloth as electrode reached 3.55 A/m² at 90 °C (Fig. 3e and fig. S9c), resulting in a peak output power of 0.4 W/m² ($P_{max} = \frac{V_{OC}I_{SC}}{4}$). As the connection between the electrodes was removed, the V_{OC} between electrodes increased to the original value within minutes (fig. S10 and fig. S11). No significant V_{OC} drop was found during the open circuit-short circuit cycles, showing great stability.

The harvested power can be applied to supply an electronic load. The current decreased with the increasing load resistance, while the voltage increased (Fig. 3f and fig. S10). The maximum output power reached its peak between 100 to 1000 Ω , corresponding to the internal resistance of the TOI composite at low frequency (Fig. 2d). It should be noted that the internal resistance of the TOI composite at low frequency can be further reduced by enhancing the interface between ionogel, hydrogel, electrode, and CEM¹⁶. The TOI composite is essentially capacitive because the discharge current is non-faradaic and no electrons transfer across the electrode-electrolyte interface. The $\text{LiNO}_3\cdot 3\text{H}_2\text{O}$ based TOI composite in this study is a proof-of-concept design, and the voltage would drop slowly in the closed circuit due to the decreasing ion gradient. To make the TOI composite work continuously and keep a constant ion gradient, redox reactions can be introduced on the electrode-electrolyte interface in future work², and the widely reported Cu/Cu^{2+} redox couples may be a good choice⁵².

Thermo-osmotic conversion efficiency

Assuming a constant ion gradient, the peak heat-to-electric energy conversion efficiency of the TOI composite (η_E) was calculated by the ratio of output electric power (P_{out}) to the input thermal power (P_{input}). The input thermal power includes the thermal diffusion (P_{diff}) in the electric power generation stage and the heat absorbed for ionic crystal transition (P_{melt}) in the corresponding ion generation stage, expressed as $P_{input} = \kappa A \frac{\Delta T}{\Delta x} + \frac{\Delta H I}{F}$, where ΔH is the enthalpy of melting, I is the current, $F = 96485 \text{ Cmol}^{-1}$ is Faraday constant, κ is the thermal conductivity of

the TOI composite, A is a cross-sectional area of the CEM, and Δx is a distance between the electrodes. The output power of the TOI composite reaches the maximum value when the output voltage is selected as half of the V_{OC} ($V_{out} = 0.5V_{oc}$), expressed as $P_{out} = \frac{V_{out}^2}{R} = \frac{\sigma_e AV_{OC}^2}{4\Delta x}$, where σ_e is the ionic conductivity of the TOI composite. Consequently, η_E can be expressed as $\eta_E = \frac{P_{out}}{P_{input}} = \frac{\sigma_e V_{OC}^2}{4(\kappa\Delta T + \frac{\Delta H\Delta x}{FA})}$ (Supplementary Text 3). Therefore, a larger differential thermal voltage ($\frac{V_{oc}}{\Delta T}$), a higher effective ionic conductivity (σ_e), a lower thermal conductivity (κ), and a smaller melting enthalpy (ΔH) will lead to a higher η_E .

Fig. 4. Peak energy conversion efficiency and comparison. (a) Heat-to-electric energy conversion efficiency versus operation temperature. (b) Carnot-relative efficiency ($\frac{\eta_E}{\eta_{Carnot}}$), where $\eta_{Carnot} = \frac{T_H - T_L}{T_H + 273.15}$. T_L is the cold-side temperature during the operation. The peak energy conversion efficiency of TOI composite is significantly higher than previously reported TEs^{3, 5, 10}, liquid thermo-electrochemical technologies such as a conventional thermo-galvanic cell (TGC)^{15-17, 19, 53}, thermosensitive crystallization–boosted liquid thermo-cell (TC-LTC)⁵⁴, thermally regenerative electrochemical cycle (TREC)^{3, 55-57}, direct thermal charging cell (DTCC)⁵, redox flow battery (RFB)^{8, 58}, thermally regenerative battery (TRB)^{18, 59-61}, osmotic heat engines (OHE)^{29, 32}, and thermo-osmotic energy conversion (TOEC)⁶².

As the supply heat went up from 40 °C to 90 °C, the differential thermal voltage of the TOI composite increased from 18 to 26 mV/K (Fig. 3c) while the thermal conductivity stabilized at around 0.588 W/m⁻¹K⁻¹ (fig. S13a)^{21, 63, 64}, and the effective ionic conductivity rose from 10.9 to 19.6 S/m (fig. S13b), resulting in an increase in the η_E of the TOI composite from 1.5% to 11.17%, which was slightly lower than the theoretical prediction of 13.6% (Supplementary Text 2)^{53, 65}. To the best of our knowledge, the peak η_E of the TOI composite at 90 °C is at least twice as efficient as the previously reported low-grade heat harvesting technologies (Fig. 4a). Notably, unlike those previously reported methods, no extra energy is needed to maintain the ΔT or pump the working fluids in as-studied TOI composite. The ratio of η_E to η_{Carnot} of the TOI composite was also changed from 40% to 65% (Fig. 4b). Specifically, the TOI composite achieved 57% of η_{Carnot} at 66 °C ($\eta_{Carnot} = 11.2\%$) and 65% of η_{Carnot} at 90 °C ($\eta_{Carnot} = 17.1\%$), showing the great economic and environmental benefits of recovering low-grade heat.

Prototype demonstration

Here we also demonstrated a prototype device based on the capacitive TOI composite operating in a quasi-continuous mode. Specifically, multiple TOI composite can be connected in series as a flexible power supply device (fig. S14). When the heat source reached 90 °C, each unit set of TOI composite contributed 0.45 V, and a device containing 8 TOI composite units produced a voltage of 3.27 V (Fig. 5a). Once the electrodes were connected by an electric circuit (short-circuit here), the thermal energy could be converted to electric energy and the voltage dropped to zero. After disconnecting the external circuit, the voltage recovered within several minutes (Fig. 5b). This flexible device can be adapted to different surfaces^{46, 47}. For example, it could absorb heat from the surface of a glass filled with hot water to power the light-emitting diode transiently (LED, $V_{working} = 1.7V$, Fig. 5c). More intriguingly, the 8-unit TOI device absorbed heat from the surface of

the human arm and powered the LED (Fig. 5d), showing its potential to power wearable devices (such as electric-skin).

5 Fig. 5. Proof-of-concept demonstration of TOI composite. (a) 8-unit TOI composites connected in series generated an open-circuit voltage of 3.27 V at 90 °C. (b) V_{oc} of 8-unit device during open-circuit and short-circuit cycles at 90 °C. (c, d) LED was powered transiently by 8-unit TOI devices through absorbing the heat from hot water or the human body.

Regenerative demonstration

10 The DSC curve of the $\text{LiNO}_3\text{-3H}_2\text{O}$ ionogel showed similar heat flow in 4 melting-recrystallization cycles (Fig. 6a). The melting enthalpy of the ionogel was maintained at around 21 kJ/mol during the 4 melting-recrystallization cycles (Fig. 6b), indicating that the TOI composites have potentially good reversibility. As the heat source is higher than the melting temperature, the crystalline ionogel can absorb heat and generate free ions. When the ionogel, hydrogel, CEM, and
15 and electrodes are assembled into TOI composite, the selective cation diffusion from the ionogel to the hydrogel generates a V_{oc} pointing from the hydrogel to ionogel. When the ambient temperature is lower than the recrystallization point (10 °C) of $\text{LiNO}_3\text{-3H}_2\text{O}$ ionogel, the molten $\text{LiNO}_3\text{-3H}_2\text{O}$ will recrystallize, which makes the cation concentration in the ionogel lower than that in the hydrogel. The reverse cation gradient can drive the cation to diffuse from the hydrogel
20 back to the ionogel, thereby reactivating the TOI composite (figs. S3d and S3e). For instance, the V_{oc} of the 8-unit TOI device dropped from 2.52 V to 0.59 V after changing the heat source from hot water (70 °C) to ice water (10 °C) (Figs. 6c and 6d). The dropped V_{oc} was due to the reduction of the charge imbalance between the ionogel and hydrogel, which proved that some cations diffused from the hydrogel back to the ionogel. The reduced V_{oc} ratio indicates the percentage of cation reverse diffusion, thus it is estimated that the feasible regeneration efficiency of the
25 TOI composite is 76.6%.

Although the DSC curve shows that the recrystallization point of the ionogel is around 10 °C, the recrystallization process can actually occur through nucleation stimulation once below the
30 melting point. Since the recrystallization of the ionogel is an exothermic process, the regeneration of TOI composite is spontaneous under melting point, thus no additional energy input is required. When the electrodes of the TOI composite were connected by an external load, a current flew from the ionogel-connected electrode to the hydrogel-connected electrode (Fig. 3d). However, due to the limited reverse Δc and low ionic conductivity in the regeneration process, this electric power was small. To effectively utilize this reverse electric power and
35 improve regenerative efficiency, additional investigation is needed. One possible solution is to establish a reverse ΔT from hydrogel to ionogel. Considering the lower ion gradient and low ion mobility, the time needed for recrystallization process is longer than the discharge process.

40 Fig. 6. Regenerative demonstration of TOI device. (a) DSC curve of $\text{LiNO}_3\text{-3H}_2\text{O}$ ionogel during 4 heating and cooling cycles. The insert images indicate that ionogel can be recrystallized as the ambient temperature is lower than the recrystallization temperature (T_R). (b) Normalized enthalpy of melting and recrystallization during 4 cycles. (c, d) V_{oc} of 8-unit TOI device using hot/ice water as heat/cooling source, indicating a feasible regenerative efficiency of 76.6%.

Conclusions

In summary, we have successfully demonstrated a new TOI approach to harvest low-grade heat with high peak conversion efficiency of 11.17%. The TOI composite synergistically combines the osmotic-driven ion diffusion and thermo-driven ion diffusion with selective permeation, resulting in a differential thermal voltage up to 26 mV/K. A prototype flexible TOI device with 8 elements showed a high open-circuit voltage up to 3.25 V when the heat source reached 90 °C. This device also powered the LED transiently by absorbing heat from hot water or the human body, thus confirming its great potential for powering wearable devices (such as sensors in the internet of things (IoT), e-skin, etc.). Further investigations are still needed for continuous and reversible operation, including the introduction of redox reaction on the electrodes and improving the regeneration efficiency of the TOI system. Nevertheless, this work opens a new door for high-efficiency harvesting low-grade heat by embedding thermo-osmotic conversion as an intermedia stage of thermo-electric conversion.

Author contributions

S.W. conceived the research. W.L., Z.Z. and S.W. designed the experiment, W.L., Y.L., Z.Z., and R.L. conducted the experiment. Y.L., W.L. and S.W. performed the theoretical derivation to explain the experimental data. W.L. and S.W. wrote the manuscript, J.Q. contributed to the interpretation of the results and revision of the manuscript. All authors discussed the results and participated in revising the manuscript.

Conflicts of interest

There are no conflicts to declare.

Acknowledgments

This work is partially supported by the National Science Foundation (CMMI-1934120, CMMI-1933679).

Notes and references

1. C. Forman, I. K. Muritala, R. Pardemann and B. Meyer, *Renewable and Sustainable Energy Reviews*, 2016, **57**, 1568-1579.
2. T. Li, X. Zhang, S. D. Lacey, R. Mi, X. Zhao, F. Jiang, J. Song, Z. Liu, G. Chen and J. Dai, *Nature materials*, 2019, **18**, 608-613.
3. S. W. Lee, Y. Yang, H.-W. Lee, H. Ghasemi, D. Kraemer, G. Chen and Y. Cui, *Nature communications*, 2014, **5**, 1-6.
4. N. Y. Yip, D. Brogioli, H. V. Hamelers and K. Nijmeijer, *Environmental science & technology*, 2016, **50**, 12072-12094.
5. X. Wang, Y.-T. Huang, C. Liu, K. Mu, K. H. Li, S. Wang, Y. Yang, L. Wang, C.-H. Su and S.-P. Feng, *Nature communications*, 2019, **10**, 1-8.
6. M. H. Dickson and M. Fanelli, *Geothermal energy: utilization and technology*, Routledge, 2013.
7. G. Liu, T. Chen, J. Xu, G. Li and K. Wang, *Journal of Materials Chemistry A*, 2020, **8**, 513-531.
8. A. D. Poletayev, I. S. McKay, W. C. Chueh and A. Majumdar, *Energy & Environmental Science*, 2018, **11**, 2964-2971.

9. M. Rahimi, A. P. Straub, F. Zhang, X. Zhu, M. Elimelech, C. A. Gorski and B. E. Logan, *Energy & Environmental Science*, 2018, **11**, 276-285.
10. W. He, D. Wang, H. Wu, Y. Xiao, Y. Zhang, D. He, Y. Feng, Y.-J. Hao, J.-F. Dong and R. Chetty, *Science*, 2019, **365**, 1418-1424.
- 5 11. M. Zebarjadi, K. Esfarjani, M. Dresselhaus, Z. Ren and G. Chen, *Energy & Environmental Science*, 2012, **5**, 5147-5162.
12. L. Wang, Z. Zhang, Y. Liu, B. Wang, L. Fang, J. Qiu, K. Zhang and S. Wang, *Nature communications*, 2018, **9**, 1-8.
13. S. Pandya, G. Velarde, L. Zhang, J. D. Wilbur, A. Smith, B. Hanrahan, C. Dames and L. W. Martin, *NPG Asia Materials*, 2019, **11**, 1-5.
- 10 14. S. Pandya, J. Wilbur, J. Kim, R. Gao, A. Dasgupta, C. Dames and L. W. Martin, *Nature materials*, 2018, **17**, 432-438.
- 15 15. R. Hu, B. A. Cola, N. Haram, J. N. Barisci, S. Lee, S. Stoughton, G. Wallace, C. Too, M. Thomas and A. Gestos, *Nano letters*, 2010, **10**, 838-846.
- 16 16. L. Zhang, T. Kim, N. Li, T. J. Kang, J. Chen, J. M. Pringle, M. Zhang, A. H. Kazim, S. Fang and C. Haines, *Advanced materials*, 2017, **29**, 1605652.
- 17 17. H. Im, T. Kim, H. Song, J. Choi, J. S. Park, R. Ovalle-Robles, H. D. Yang, K. D. Kihm, R. H. Baughman and H. H. Lee, *Nature communications*, 2016, **7**, 1-9.
- 18 18. F. Zhang, J. Liu, W. Yang and B. E. Logan, *Energy & Environmental Science*, 2015, **8**, 343-349.
- 20 19. C.-G. Han, X. Qian, Q. Li, B. Deng, Y. Zhu, Z. Han, W. Zhang, W. Wang, S.-P. Feng and G. Chen, *Science*, 2020, **368**, 1091-1098.
- 20 20. J. K. Platten, 2006.
- 21 21. P. J. Shamberger and T. Reid, *Journal of Chemical & Engineering Data*, 2012, **57**, 1404-1411.
- 25 22. T. B. Schroeder, A. Guha, A. Lamoureux, G. VanRenterghem, D. Sept, M. Shtein, J. Yang and M. Mayer, *Nature*, 2017, **552**, 214-218.
23. A. Siria, M.-L. Bocquet and L. Bocquet, *Nature Reviews Chemistry*, 2017, **1**, 0091.
- 24 24. K. Chen, L. Yao, F. Yan, S. Liu, R. Yang and B. Su, *Journal of Materials Chemistry A*, 2019, **7**, 25258-25261.
- 30 25. M. Macha, S. Marion, V. V. Nandigana and A. Radenovic, *Nature Reviews Materials*, 2019, **1**.
- 26 26. J. Ji, Q. Kang, Y. Zhou, Y. Feng, X. Chen, J. Yuan, W. Guo, Y. Wei and L. Jiang, *Advanced Functional Materials*, 2017, **27**, 1603623.
- 35 27. L. Ding, D. Xiao, Z. Lu, J. Deng, Y. Wei, J. Caro and H. Wang, *Angewandte Chemie*, 2020, **132**, 8798-8804.
- 28 28. D.-K. Kim, C. Duan, Y.-F. Chen and A. Majumdar, *Microfluidics and Nanofluidics*, 2010, **9**, 1215-1224.
- 29 29. R. Long, B. Li, Z. Liu and W. Liu, *Journal of membrane science*, 2017, **525**, 107-115.
- 40 30. S. Lin, N. Y. Yip, T. Y. Cath, C. O. Osuji and M. Elimelech, *Environmental science & technology*, 2014, **48**, 5306-5313.
- 31 31. P. Yang, K. Liu, Q. Chen, J. Li, J. Duan, G. Xue, Z. Xu, W. Xie and J. Zhou, *Energy & Environmental Science*, 2017, **10**, 1923-1927.
- 32 32. R. Long, Y. Zhao, Z. Luo, L. Li, Z. Liu and W. Liu, *Energy*, 2020, **195**, 117042.
- 45 33. F. J. Arias, *International Journal of Thermal Sciences*, 2018, **133**, 151-161.
- 34 34. R. D. Cusick, Y. Kim and B. E. Logan, *Science*, 2012, **335**, 1474-1477.

35. M. Dupont, D. MacFarlane and J. Pringle, *Chemical communications*, 2017, **53**, 6288-6302.
36. A. Campbell, G. Debus and E. Kartzmark, *Canadian Journal of Chemistry*, 1955, **33**, 1508-1514.
- 5 37. Z. Zhang, C. Zuo, Z. Liu, Y. Yu, Y. Zuo and Y. Song, *Journal of Power Sources*, 2014, **251**, 470-475.
38. C.-J. Lee, H. Wu, Y. Hu, M. Young, H. Wang, D. Lynch, F. Xu, H. Cong and G. Cheng, *ACS applied materials & interfaces*, 2018, **10**, 5845-5852.
39. L. Garrido, I. Aranaz, A. Gallardo, C. García, N. García, E. Benito and J. Guzmán, *The Journal of Physical Chemistry B*, 2018, **122**, 8301-8308.
- 10 40. R. Senthil and M. Cheralathan, *International Journal of ChemTech Research*, 2016, **9**, 563-570.
41. P. Karimineghlani, E. Emmons, M. J. Green, P. Shamberger and S. A. Sukhishvili, *Journal of Materials Chemistry A*, 2017, **5**, 12474-12482.
- 15 42. W. J. Xie, Z. Zhang and Y. Q. Gao, *The Journal of Physical Chemistry B*, 2016, **120**, 2343-2351.
43. W. Liu, S. W. Lee, D. Lin, F. Shi, S. Wang, A. D. Sendek and Y. Cui, *Nature energy*, 2017, **2**, 1-7.
44. M. Oldenburger, B. Beduerftig, A. Gruhle, F. Grimsman, E. Richter, R. Findeisen and A. Hintennach, *Journal of Energy Storage*, 2019, **21**, 272-280.
- 20 45. H. Cheng, X. He, Z. Fan and J. Ouyang, *Advanced Energy Materials*, 2019, **9**, 1901085.
46. Q. Jiang, H. Sun, D. Zhao, F. Zhang, D. Hu, F. Jiao, L. Qin, V. Linseis, S. Fabiano and X. Crispin, *Advanced Materials*, 2020, **32**, 2002752.
47. Y. Liu, S. Zhang, Y. Zhou, M. A. Buckingham, L. Aldous, P. C. Sherrell, G. G. Wallace, G. Ryder, S. Faisal and D. L. Officer, *Advanced Energy Materials*, 2020, **10**, 2002539.
- 25 48. T. S. Mathis, N. Kurra, X. Wang, D. Pinto, P. Simon and Y. Gogotsi, *Advanced Energy Materials*, 2019, **9**, 1902007.
49. N. Elgrishi, K. J. Rountree, B. D. McCarthy, E. S. Rountree, T. T. Eisenhart and J. L. Dempsey, *Journal of Chemical Education*, 2018, **95**, 197-206.
- 30 50. D. Zhao, A. Martinelli, A. Willfahrt, T. Fischer, D. Bernin, Z. U. Khan, M. Shahi, J. Brill, M. P. Jonsson and S. Fabiano, *Nature communications*, 2019, **10**, 1-8.
51. J. Wang, S.-P. Feng, Y. Yang, N. Y. Hau, M. Munro, E. Ferreira-Yang and G. Chen, *Nano letters*, 2015, **15**, 5784-5790.
52. W. Wang, G. Shu, X. Zhu and H. Tian, *Journal of Materials Chemistry A*, 2020, **8**, 12351-12360.
- 35 53. H. Zhou and P. Liu, *ACS Applied Energy Materials*, 2018, **1**, 1424-1428.
54. B. Yu, J. Duan, H. Cong, W. Xie, R. Liu, X. Zhuang, H. Wang, B. Qi, M. Xu and Z. L. Wang, *Science*, 2020, **370**, 342-346.
55. Y. Yang, J. Loomis, H. Ghasemi, S. W. Lee, Y. J. Wang, Y. Cui and G. Chen, *Nano letters*, 2014, **14**, 6578-6583.
- 40 56. Y. Yang, S. W. Lee, H. Ghasemi, J. Loomis, X. Li, D. Kraemer, G. Zheng, Y. Cui and G. Chen, *Proceedings of the National Academy of Sciences*, 2014, **111**, 17011-17016.
57. C. Cheng, S. Wang, P. Tan, Y. Dai, J. Yu, R. Cheng, S.-P. Feng and M. Ni, *ACS Energy Letters*, 2020, **6**, 329-336.
- 45 58. I. Facchinetti, E. Cobani, D. Brogioli, F. La Mantia and R. Ruffo, *ChemSusChem*, 2020, **13**, 5340-5340.

59. X. Zhu, M. Rahimi, C. A. Gorski and B. Logan, *ChemSusChem*, 2016, **9**, 873-879.
60. V. M. Palakkal, T. Nguyen, P. Nguyen, M. Chernova, J. E. Rubio, G. Venugopalan, M. Hatzell, X. Zhu and C. G. Arges, *ACS Applied Energy Materials*, 2020, **3**, 4787-4798.
- 5 61. W. Wang, G. Shu, H. Tian, D. Huo and X. Zhu, *Journal of Power Sources*, 2019, **424**, 184-192.
62. A. P. Straub and M. Elimelech, *Environmental science & technology*, 2017, **51**, 12925-12937.
63. N. Tang, Z. Peng, R. Guo, M. An, X. Chen, X. Li, N. Yang and J. Zang, *Polymers*, 2017, **9**, 688.
- 10 64. O. U. Rehman and A. F. Zafar, *Journal of Electrochemical Science and Engineering*, 2017, **7**, 223-235.
65. I. Prigogine, *itti*, 1967.

15

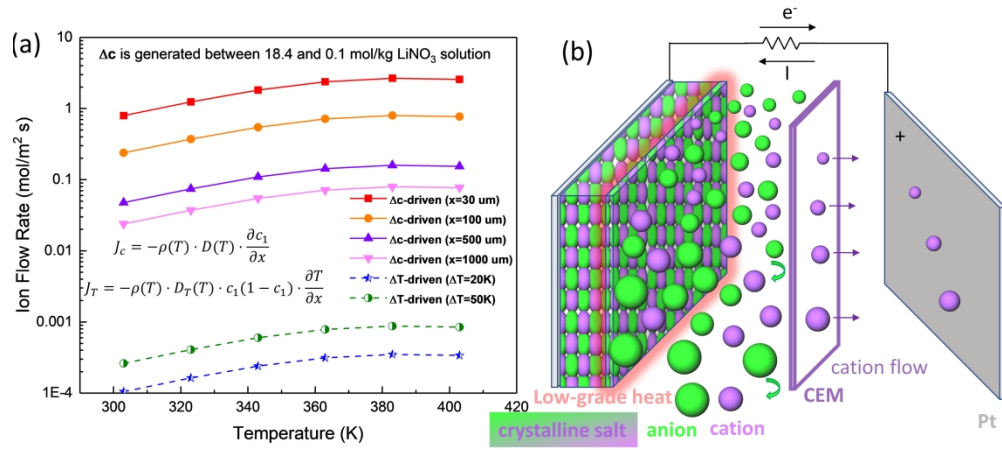


Fig. 1. Fig. 1. Concept and working principle of the TOI approach. (a) Comparison of ion flow rate driven by ion gradient (Δc) and temperature gradient (ΔT). The results are calculated based on the Soret coefficient, where Δc is produced between LiNO₃·3H₂O (18.4 mol/kg) and 0.1 M LiNO₃ solution. x represents the thickness of the separation membrane. J_c and J_T are the ion flow rate driven by Δc and ΔT , respectively. (b) Illustration of a proposed TOI composite, which converts low-grade heat into Δc by melting the crystalline salt hydrate, and then generates electric energy through ion diffusion and selective permeation.

293x131mm (300 x 300 DPI)

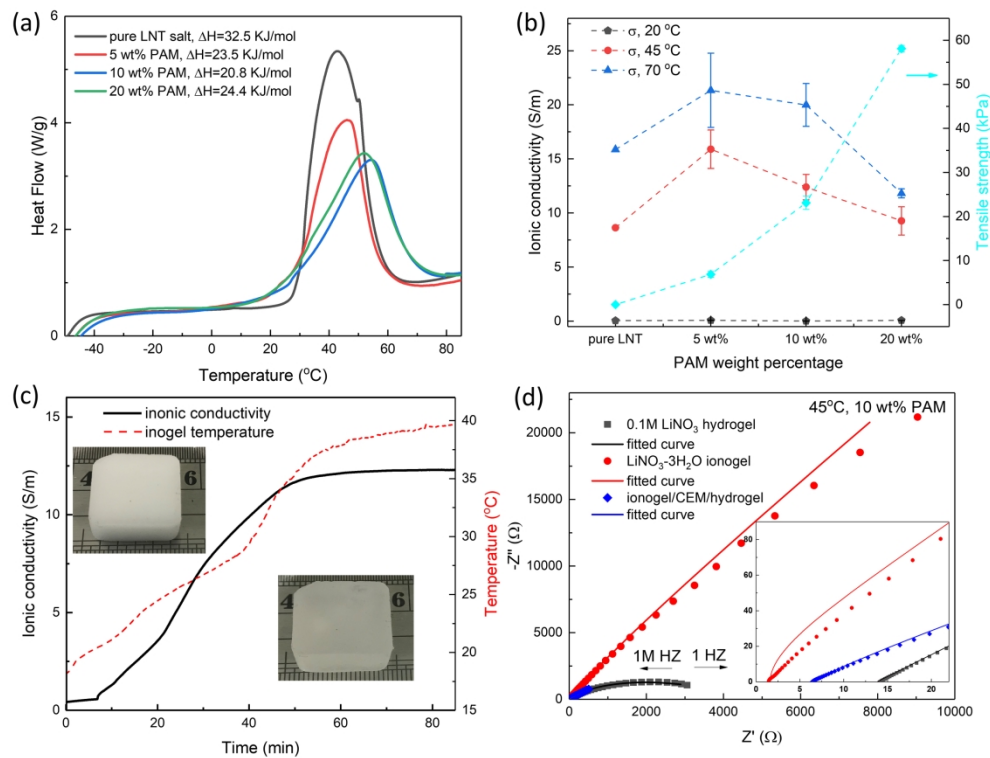


Fig. 2. Characterization of ionogels and heat-induced ion gradient generation. (a) DSC curve and normalized melting enthalpy of LiNO₃·3H₂O in ionogels with various PAM concentrations. (b) Ionic conductivity and tensile strength of LiNO₃·3H₂O ionogel as a function of PAM concentrations. (c) The real-time phase transition and ion generation of crystalline LiNO₃·3H₂O ionogel as a function of heating time and temperature (Left insert: unheated crystalline ionogel, Right insert: heated molten ionogel). (d) Measured and fitted impedance spectra of the 0.1M LiNO₃ hydrogel, LiNO₃·3H₂O ionogel, and ionogel/CEM/hydrogel composite at 45 °C. The inset shows the zoomed view in the high-frequency region.

233x179mm (300 x 300 DPI)

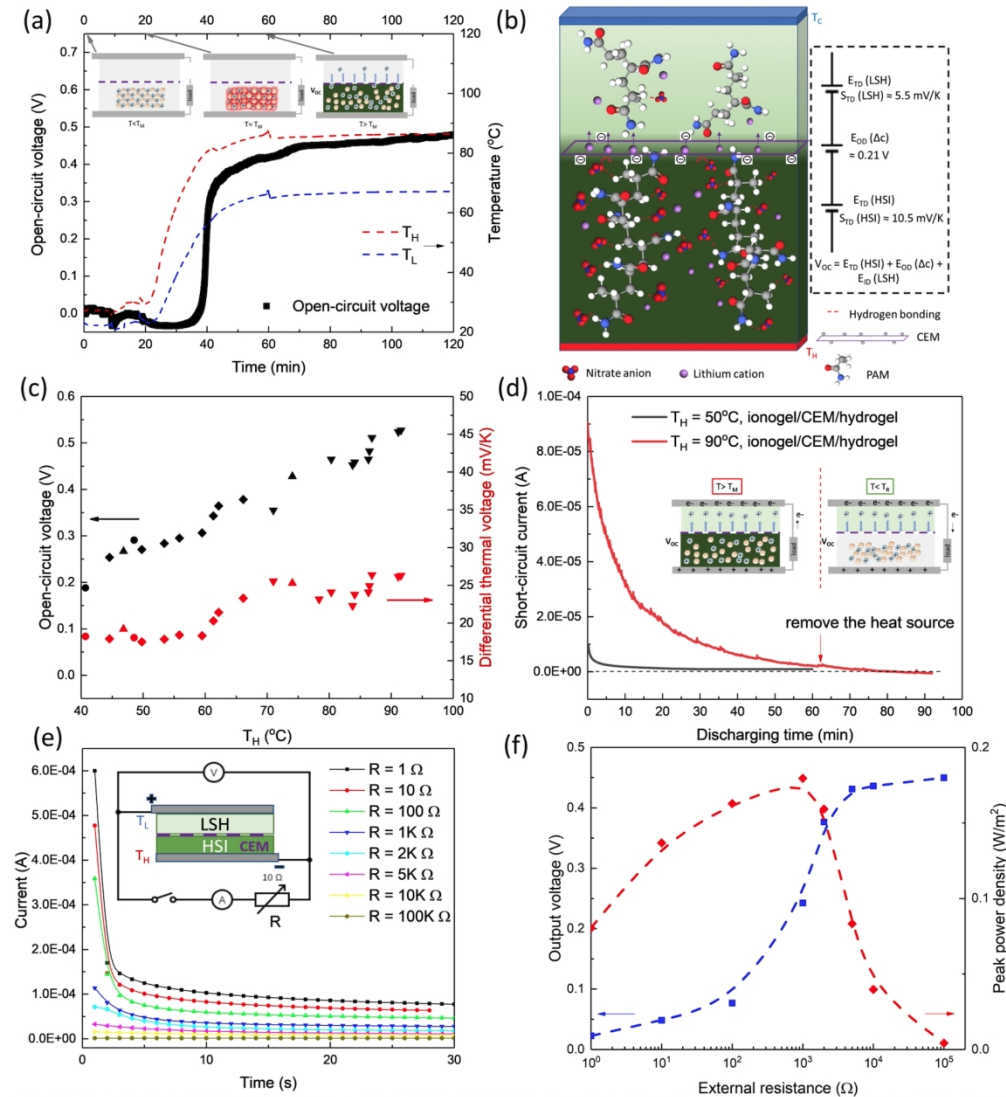


Fig. 3. Electrical power generation of TOI composite. (a) Real-time recording of the V_{OC} and hot/cold side temperature of TOI composite as the heat source stayed at 88 °C. (b) Voltage generation mechanism of the TOI approach, osmotic-driven and thermo-driven ion diffusion integrated with selective permeation. The enhanced cation selectivity of the TOI system is ascribed to the intermolecular hydrogen bonding between nitrate anion and densely hydrophilic amide group, along with the thermo-mobility difference of nitrate anion and lithium cation. (c) V_{OC} and differential thermal voltage of TOI composite as a function of the temperature of heat source. (d) Short-circuit current of TOI system as a function of time during discharging. (e) Current of the discharge process at the different external resistors. The inset shows the measurement circuit. (f) Corresponding output voltage and peak power density at the different external resistors.

639x705mm (72 x 72 DPI)

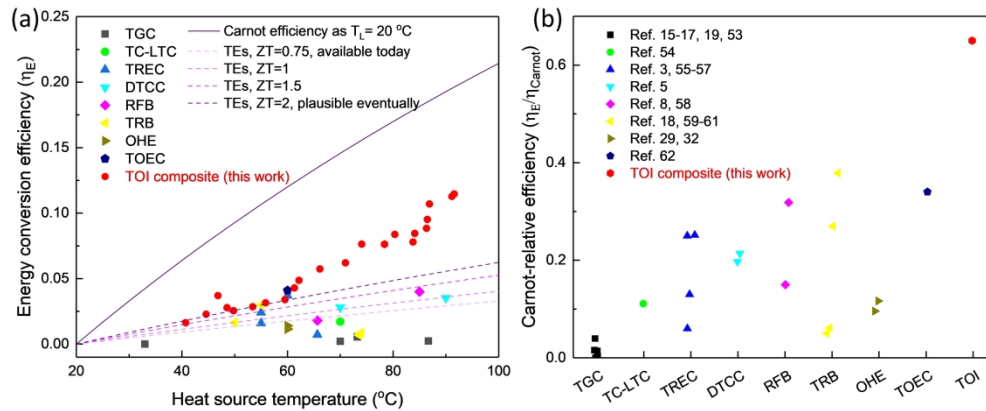


Fig. 4. Peak energy conversion efficiency and comparison. (a) Heat-to-electric energy conversion efficiency versus operation temperature. (b) Carnot-relative efficiency ($\eta_E/\eta_{\text{Carnot}}$), where $\eta_{\text{Carnot}} = (T_H - T_L)/(T_H + 273.15)$. T_L is the cold-side temperature during the operation. The peak energy conversion efficiency of TOI composite is significantly higher than previously reported TEs 3, 5, 10, liquid thermo-electrochemical technologies such as a conventional thermo-galvanic cell (TGC) 15-17, 19, 53, thermosensitive crystallization-boosted liquid thermo-cell (TC-LTC) 54, thermally regenerative electrochemical cycle (TREC) 3, 55-57, direct thermal charging cell (DTCC) 5, redox flow battery (RFB) 8, 58, thermally regenerative battery (TRB) 18, 59-61, osmotic heat engines (OHE) 29, 32, and thermo-osmotic energy conversion (TOEC) 62.

261x108mm (300 x 300 DPI)

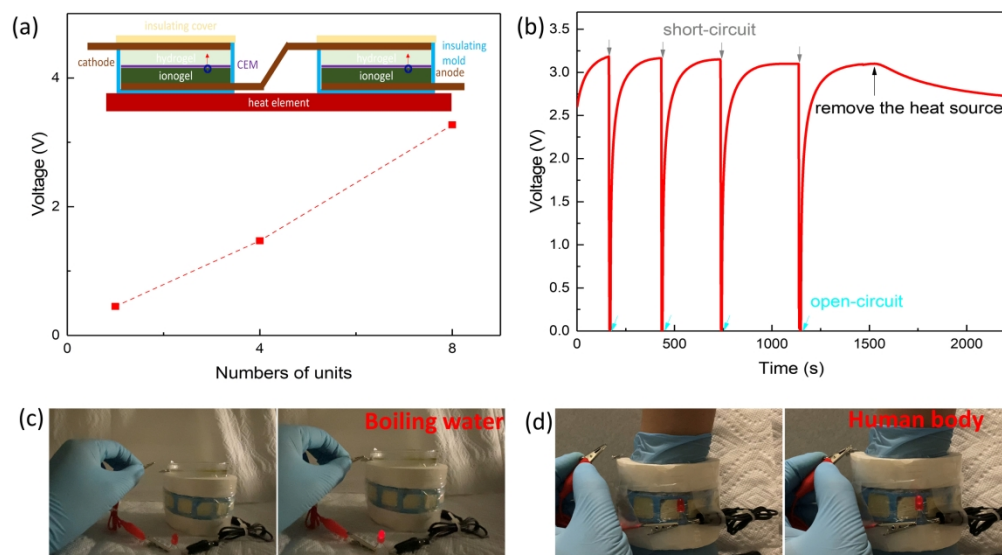


Fig. 5. Proof-of-concept demonstration of TOI composite. (a) 8-unit TOI composites connected in series generated an open-circuit voltage of 3.27 V at 90 °C. (b) V_{oc} of 8-unit device during open-circuit and short-circuit cycles at 90 °C. (c, d) LED was powered transiently by 8-unit TOI devices through absorbing the heat from hot water or the human body.

248x138mm (300 x 300 DPI)

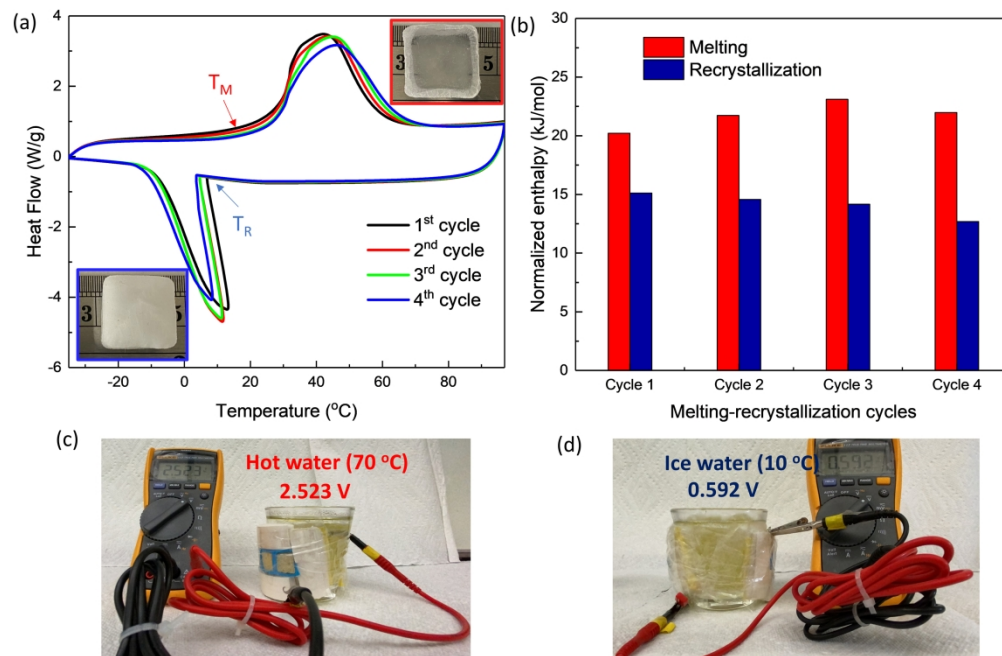


Fig. 6. Regenerative demonstration of TOI device. (a) DSC curve of LiNO₃-3H₂O ionogel during 4 heating and cooling cycles. The insert images indicate that ionogel can be recrystallized as the ambient temperature is lower than the recrystallization temperature (T_R). (b) Normalized enthalpy of melting and recrystallization during 4 cycles. (c, d) VOC of 8-unit TOI device using hot/ice water as heat/cooling source, indicating a feasible regenerative efficiency of 76.6%.

277x182mm (300 x 300 DPI)